

## Toward quantifying uncertainty in travel time tomography using the null-space shuttle

R. W. L. de Wit,<sup>1</sup> J. Trampert,<sup>1</sup> and R. D. van der Hilst<sup>2</sup>

Received 27 August 2011; revised 9 December 2011; accepted 28 December 2011; published 3 March 2012.

[1] The solution of large linear tomographic inverse problems is fundamentally non-unique. We suggest to explore the non-uniqueness explicitly by examining the null-space of the forward operator. We show that with the null-space shuttle it is possible to assess robustness in tomographic models, and we illustrate the concept for the global P-wave model MIT-P08. We found a broad range of acceptable solutions compatible with the travel time data. The root mean square (RMS) velocity perturbations vary from 0.2 to 0.6% in the lowermost mantle and from 0.3 to 1.3% in the upper mantle. Such large variations in average amplitudes prohibit meaningful inferences on temperature or chemical variations in the Earth from tomographic models alone. On a global scale much short wavelength structure resides in the null-space of the forward operator, suggesting that the data do not everywhere resolve structure on the smallest length scale (<200 km) allowed by the (block) parameterization used in MIT-P08 and similar models. This indicates that great care should be taken when interpreting such structure. As a practical measure, we suggest that only those structures for which the wave speed perturbations do not change sign within the range of models permitted by the data should be considered robust. With this criterion, the model null-space analysis shows that the high velocity anomalies in the lower mantle, which are often interpreted as remnants of slabs of subducted lithosphere, are required by the seismic data. Low-velocity anomalies underneath, for instance, Hawaii, Iceland, and Africa show varying degrees of robustness.

**Citation:** de Wit, R. W. L., J. Trampert, and R. D. van der Hilst (2012), Toward quantifying uncertainty in travel time tomography using the null-space shuttle, *J. Geophys. Res.*, 117, B03301, doi:10.1029/2011JB008754.

### 1. Introduction

[2] The ever increasing quantity of seismic data from both global and regional networks enables global body wave travel time tomography to constrain velocity variations within the Earth with increasing detail [e.g., *Dziewonski et al.*, 1977; *Vasco and Johnson*, 1998; *Bijwaard and Spakman*, 2000; *Kárason and van der Hilst*, 2000; *Grand*, 2002; *Widiyantoro et al.*, 2001; *Zhao*, 2004; *Li et al.*, 2008]. In most such studies, however, more attention is paid to interpretation than to analyzing the quality of the tomographic models. To assess a model, a quantitative study of uncertainty is needed [*Trampert and van der Hilst*, 2005]. The solution of tomographic inversions is fundamentally non-unique and, in general, the quality of a tomographic image is limited by the quality of the data, the data coverage and the approximations made in the formulation of both the forward and inverse problem. The data used in travel time

tomography typically suffer from an uneven sampling of the Earth's interior by body waves. Furthermore, the travel time data include both random and systematic errors that are difficult or even impossible to estimate accurately, although attempts have been made [e.g., *Gudmundsson et al.*, 1990; *Röhm et al.*, 1999].

[3] The performance of inversions of synthetic data calculated from a known input model is often used as a proxy for the quality of a tomographic image. Most popular are the so-called checkerboard tests, in which synthetic data are computed from a regular pattern of positive and negative wave speed values, but such tests are actually of limited diagnostic value [*Lévêque et al.*, 1993; *van der Hilst et al.*, 1993]. More useful are so-called 'hypothesis tests' in which the ability of data to resolve the structural features of particular interest is tested through inversion of synthetic data calculated for a series of alternative or competing models [e.g., *Spakman et al.*, 1989; *van der Hilst et al.*, 1997; *Bijwaard et al.*, 1998; *Wolfe et al.*, 2002; *Montelli et al.*, 2004]. Such tests help gain confidence in specific features, and they can be used to show, for instance, that travel time inversion with local basis functions can resolve long wavelength structures identified in models represented by spherical harmonics [e.g., *van der Hilst et al.*,

<sup>1</sup>Department of Earth Sciences, Utrecht University, Utrecht, Netherlands.

<sup>2</sup>Department of Earth, Atmospheric, and Planetary Sciences, Massachusetts Institute of Technology, Cambridge, Massachusetts, USA.

1997], but they do not yield a quantitative measure of the quality of the entire solution or the uncertainty of individual model parameters.

[4] To obtain more quantitative measures of the uncertainty in model parameters one can calculate the associated resolution [Aki *et al.*, 1977; Boschi, 2003] and covariance matrices [Vasco *et al.*, 2003; Soldati *et al.*, 2006]. Resolution matrices are useful as they give an unambiguous picture of the linear dependencies between individual model parameters. Current computer facilities allow us to calculate such matrices [Trampert and Lévêque, 1990; Soldati and Boschi, 2005], but the visualization and interpretation of a matrix with a dimension of the order of several hundred thousand is still a challenge. Covariance matrices are useful if data and prior model covariances are known and based on the physics of the problem. But this is rarely the case. Indeed, one often uses mathematical regularization and smoothness constraints, which can lead to covariances that grossly misrepresent uncertainty.

[5] In view of the non-uniqueness of solutions, model uncertainty should be inferred from the ensemble of models that, given the uncertainties in the data, fit the data within a given misfit tolerance. Such an ensemble can be found by forward sampling [e.g., Resovsky and Trampert, 2003], but current computers can only achieve this for modest size inverse problems, that is, of the order of 10 to 100 model parameters. Larger problems rely on linearization and only allow one to study the data misfit locally. The covariance can then be interpreted as the width of the misfit function when the data change within their uncertainties. In the Bayesian context, this width is given by the inverse Hessian of the problem [e.g., Tarantola, 2005] which strongly depends on the chosen regularization. A strong regularization will automatically yield an optimistically small model uncertainty, whereas smoothing will give a very large uncertainty because in that case the inverse regularization operator is rank deficient.

[6] Meju [2009] proposed to find the range of acceptable models given a fixed tolerance on the misfit function. His method relies on a quadratic approximation of the misfit function, however, and the optimal solution –and, thus, the range– depends again on the inverse Hessian, with the drawbacks mentioned above.

[7] Because of the fundamental non-uniqueness of the solution the misfit function is flat and a local quadratic approximation might be inappropriate. We suggest to address non-uniqueness explicitly by taking the null-space of the forward operator into account when analyzing model uncertainty. Deal and Nolet [1996] designed the null-space shuttle to exploit components of the model null-space, in combination with physical *a priori* information, to enhance the corresponding tomographic image [Deal *et al.*, 1999]. In doing so, the null-space shuttle can be viewed as a tool for hypothesis testing that is more efficient and more quantitative than the common resolution tests mentioned above. We generalize the null-space shuttle and use it to assess robustness in the type of travel time tomographic model produced by, for instance, Fukao *et al.* [1992, 2001], van der Hilst *et al.* [1997], Bijwaard *et al.* [1998], Vasco and Johnson [1998], Kárason and van der Hilst [2001], Zhao [2004], and Montelli *et al.* [2004]. Our method is comparable to Meju's extremal bound analysis but does not explicitly use

the inverse Hessian. The bounds are evaluated using scaled null-space components. For illustration purposes we use the P-wave model by Li *et al.* [2008], hereinafter MIT-P08. We emphasize, however that the conclusions about model uncertainty are pertinent to other P and S travel time models as well, perhaps even more so since MIT-P08 is based on a more comprehensive data set than most other models. The conclusions might be different for S-wave models, especially if surface wave dispersion data are included, but the proposed technique is general and is applicable to any linearized tomographic inverse problem.

[8] Since tomographic models are rarely minimum norm models, they contain a null-space component. We will use the null-space shuttle to show how to extract this component and evaluate the robustness of a tomographic model. We will show a range of models that –within a given data misfit tolerance– fit the data equally well as MIT-P08, and we discuss first-order implications for the interpretation in terms of deep subduction, upwellings of mantle plumes, and variations in temperature and chemical composition.

## 2. Data and Their Uncertainties

[9] The data used by Li *et al.* [2008] consist of residuals with respect to travel times computed from *ak135* [Kennett *et al.*, 1995] from three sources: (1) more than ten million routinely picked and processed travel times from global and regional networks; (2) more than twenty thousand differential times measured by waveform cross correlation; and (3) about two hundred thousand phase arrivals from temporary arrays. For internal consistency, all data are processed and used for earthquake hypocenter determination using the algorithms due to Engdahl *et al.* [1998], which hereinafter will be referred to as EHB. For further details on the data used we refer the reader to Li *et al.* [2008], and for a discussion of the different weights used we refer to Kárason and van der Hilst [2001].

[10] The seismic data represented in, for instance the catalog of the International Seismological Centre (ISC), which were reprocessed by Engdahl *et al.* [1998], have varying precision. It is, therefore, difficult to obtain a reliable estimate of the uncertainties in the millions of data available for travel time tomography. Knowledge of these uncertainties is important, however, when judging the significance of a certain data misfit. A few studies have attempted to estimate the observational errors in the ISC database. Gudmundsson *et al.* [1990] estimated errors in teleseismic ISC delay times by performing statistical tests and find a mean value of 0.5 s, while Amaru *et al.* [2008] approximate the RMS picking error in the ISC data to be 0.75 s. Reading or picking errors are assumed to be random and can therefore be reduced through stacking, for instance by constructing composite rays [Spakman and Nolet, 1988], but this is not the case for systematic errors in a dataset. Röhm *et al.* [1999] tested delay times of the EHB database for systematic variations in time. They find temporal variations of the median delay time of 0.5–1.0 s, in agreement with Grand [1990] who reported a late arrival bias in the ISC data of 0.5 s depending on the gain of stations. Because of their systematic nature, Röhm *et al.* [1999] expect that these errors will not necessarily cancel out by using the large number of

travel times in the ISC Bulletin, which may cause a bias in the tomographic images.

### 3. Null-Space Shuttle

[11] We follow the inversion procedure as described by *Li et al.* [2008], who construct a global model of P-wave velocity perturbations in the Earth's mantle. The model consists of blocks of constant slowness (the inverse of wave speed) and parameters associated with source relocation. We omit the 3D crustal correction because it introduces a bias in the estimated null-space component due to the way the crustal correction is implemented via regularization. Removing this crustal correction influences neither the stability of the inversion nor the results presented in this report. All solutions presented here were obtained after 100 iterations of the LSQR algorithm [*Paige and Saunders*, 1982], after which most of the misfit reduction was accomplished.

[12] We consider a model  $m_d$  that results from inversion of the recorded data  $d$ , that is  $m_d = Ld$ , with  $L$  some generalized inverse operator. We further consider a test model  $m_t$  that may be close to  $m_d$  but which does not necessarily explain the data. In general,  $m_t$  has components both in the range and in the null-space of a forward operator  $G$ , so that

$$m_t = m_t^{range} + m_t^{null}. \quad (1)$$

The part of  $m_t$  lying in the null-space of the forward operator  $G$  has no effect on the data misfit and can be found using the null-space shuttle as proposed by *Deal and Nolet* [1996]. Defining

$$Gm_t = d_t, \quad (2)$$

with  $d_t$  the synthetic data vector corresponding to  $m_t$ , gives

$$Gm_t^{range} = d_t, \quad (3)$$

because  $Gm_t^{null} = 0$  by definition. Solving the inverse problem for  $m_t$  in equation (3) yields  $m_t^{range}$  and it is (in principle) straightforward to obtain  $m_t^{null}$  via equation (1). To do so, we employ the same LSQR algorithm as is used to solve the original inverse problem. We note that we would obtain  $m_t^{range}$  exactly if the algorithm used to solve the inverse problem provides a minimum norm solution. A minimum norm solution fits the data exactly and has no components in the model null-space. However, due to the necessary regularization the solution to our inverse problem, and most others, is a compromise between the minimum norm and the least-squares solution. Therefore, we only get an estimate:

$$\tilde{m}_t^{range} = Ld_t = Rm_t, \quad (4)$$

with  $L$  the inverse operator corresponding to the LSQR algorithm and  $R$  the resolution operator. In our notation,  $\tilde{m}_t$  refers to estimated model parameters and  $\tilde{m}_t^{range}$  is different from but close to  $m_t^{range}$ . Consequently, we have a good approximation of the null-space component of  $m_t$ :

$$\tilde{m}_t^{null} = m_t - \tilde{m}_t^{range} = (I - R)m_t. \quad (5)$$

For a perfect resolution, that is,  $R = I$ , there is no model null-space.

[13] Let us now consider again the original solution  $m_d$ . Once the null-space component of  $m_t$  has been calculated via the approximate null-space operator  $I - R$ , we may define a new solution

$$\tilde{m}_{new} = m_d + \alpha \tilde{m}_t^{null}, \quad (6)$$

with  $\alpha$  a scaling factor. Since  $G\tilde{m}_t^{null}$  is not exactly zero, the new solution in equation (6) corresponds to a slightly different data misfit than the original solution  $m_d$ . However, as will be shown below, effects on the data misfit are small compared to presumed data uncertainties. The null-space shuttle therefore provides us with a powerful tool to investigate the robustness of a tomographic model in a straightforward fashion.

[14] A full exploration of the model null-space is practically impossible as one would have to evaluate an infinite number of test models ( $m_t$  in equation (6)). Therefore, we need to focus our analysis on a certain subset of test models. For instance, we could choose a test model consisting of random anomalies, for which we would analyze the uncertainties on the scale of the raw model parameters, i.e. single constant-slowness blocks. At the other end of the spectrum, using a uniform test model, we could explore the model null-space on the length scale of the complete Earth model.

### 4. Results

[15] In this study we obtain a set of new solutions by projecting the original tomographic image  $m_d$  (Figure 1) onto the model null-space; that is, we use  $m_d$  as a test model. By using the null-space component of the original solution we implicitly assess its robustness with the same resolution as the original model.

[16] We use the null-space shuttle to infer quantitative bounds for the tomographic model and construct a range of acceptable models, that is, models that explain the data within a chosen data misfit tolerance. In the process we will obtain a model that, for a given regularization, approximates the minimum norm solution and therefore only contains structures required by the data.

[17] In the Bayesian framework, and assuming Gaussian statistics, the approximate null-space operator  $I - R$  equals  $C_{\bar{m}}C_m^{-1}$  [*Tarantola*, 2005], where  $C_{\bar{m}}$  is the posterior and  $C_m$  the prior model covariance. That is,  $I - R$  can be seen as a relative covariance. Although we are not working in a Bayesian context, we propose to use equation (6) applied to the tomographic model  $m_d$  itself, that is,  $m_t = m_d$ , as a basis for analyzing the range of possible models. We then get, from equation (6),

$$\delta m = \tilde{m}_{new} - m_d = \alpha \tilde{m}_d^{null} = \alpha(I - R)m_d, \quad (7)$$

where  $\alpha$  is some numerical factor chosen to obtain a pre-defined deviation for the data misfit. For a given  $\alpha$ ,  $\alpha(I - R)$  presents a relative deviation from the original model  $m_d$ . We recall that  $\tilde{m}_t^{null}$  is not exactly in the model null-space and that  $I - R$  increases from zero (that is, perfect resolution) with decreasing resolution.

[18] It is essential to define a tolerance on the data misfit. The root mean square (RMS) of the data misfit prior to inversion is 1.92 s, while the RMS data misfit for the

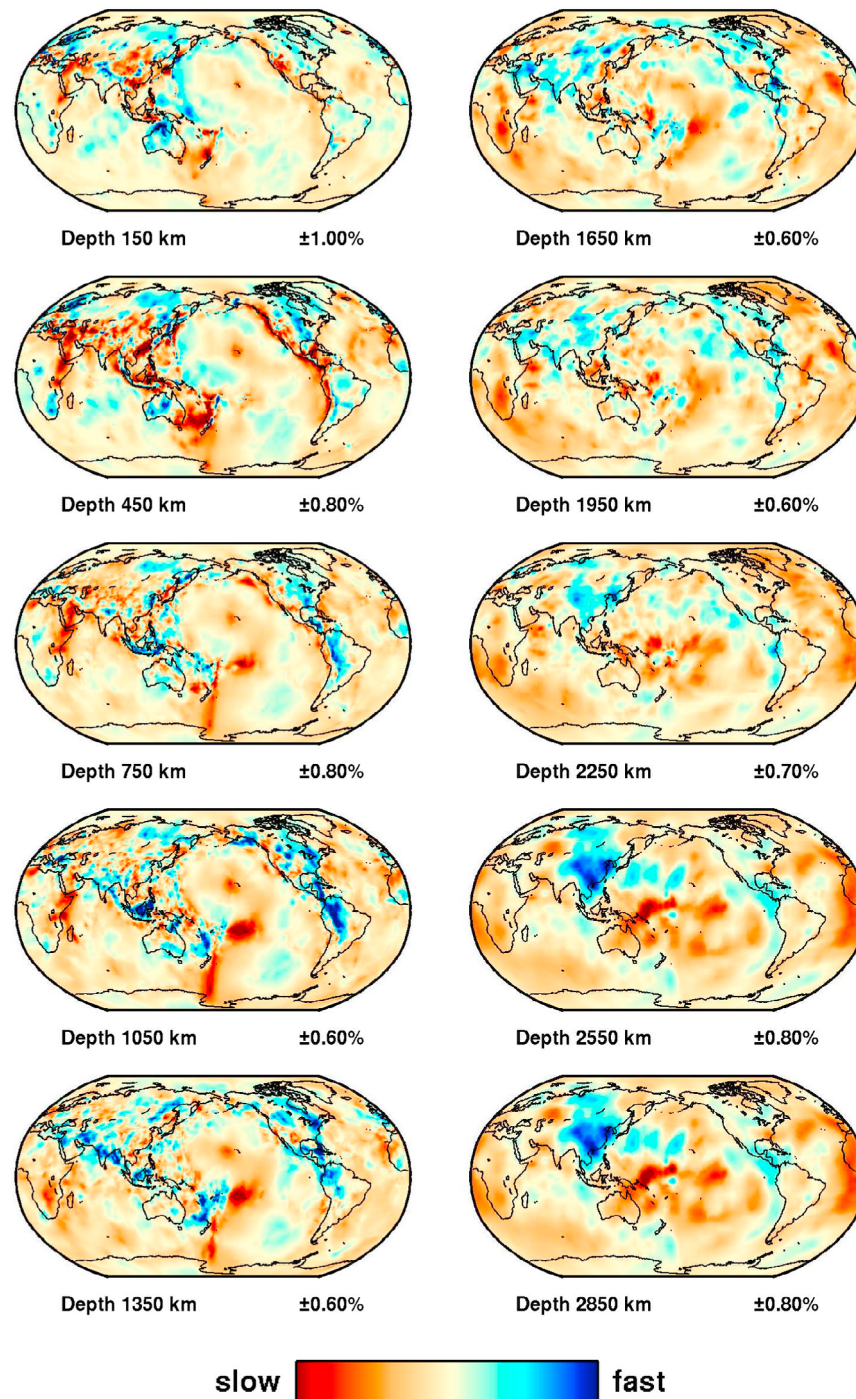


**Figure 1.** The original P wave speed perturbation model MIT-P08 without a crustal correction. The perturbations are in percent with respect to  $ak135$ . The color scale is different for each depth slice and the corresponding amplitude range is given at the bottom right beneath each panel.

original tomographic image is 1.46 s, corresponding to a variance reduction of 42%. This suggests that the average of reported values for uncertainty in ISC picks  $-0.5$  s [Grand, 1990; Gudmundsson *et al.*, 1990; Röhm *et al.*, 1999]– is more than the achieved misfit reduction during the inversion. We should not forget, however, that the inversion was formulated for composite rays and after (non-linear) relocation and phase re-identification [Engdahl *et al.*, 1998] and not for

the original (individual) ISC travel time picks. Assuming that errors in the data are random, we divide this uncertainty by  $\sqrt{10}$  because on average 10 rays were used to construct a single composite ray. This would yield an estimate for the (composite ray) data uncertainty of 0.1 s, but because part of the error in the EHB data may be systematic [Röhm *et al.*, 1999] this value may underestimate the actual data uncertainty. For example, in their tomographic study of the mantle

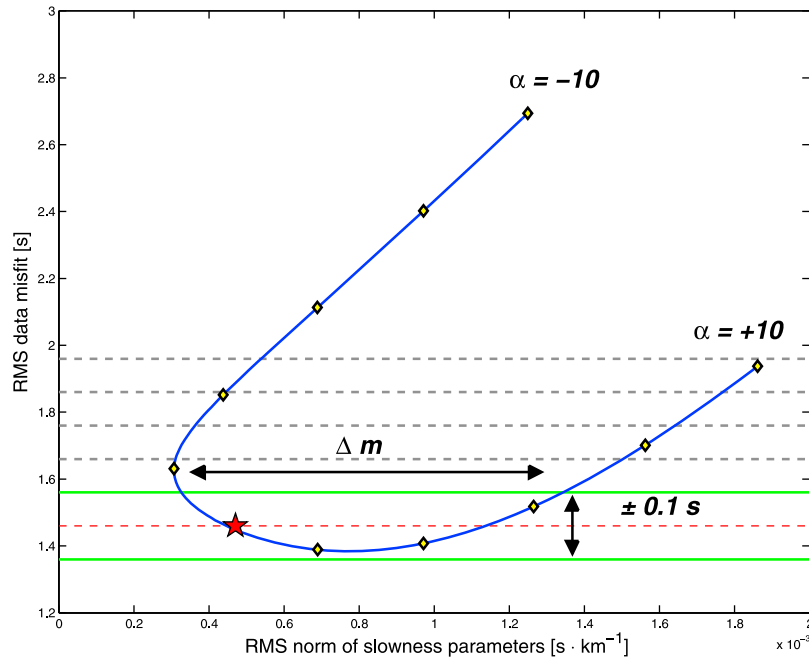


**Figure 2.** RMS data misfit of the tomographic solution versus RMS norm of the slowness parameters in the tomographic solution. Red star denotes the original solution  $m_d$ . Yellow diamonds represent the scaling factor  $\alpha$  from  $-10$  to  $10$  with an interval of  $2$ . Green lines represent the  $\pm 0.1$  s tolerance on the RMS data misfit defined in the text. Grey dashed lines represent changes in the data misfit from  $0.2$  to  $0.5$  s (upward) with  $0.1$  s intervals.

beneath the NW Pacific, *van der Hilst et al.* [1993] report a smaller effect on variance reduction of summary ray construction: compared to the original ISC picks selected for the region (RMS  $1.5$  s), the data variance was reduced by  $17\%$  upon EHB relocation, a further  $14\%$  upon summary ray construction, and another  $42\%$  upon inversion of the summary ray data, for a total RMS reduction of  $0.6$  s.

[19] Figure 2 shows the RMS data misfit versus RMS norm of  $\tilde{m}^{new}$  (slowness parameters only) for new solutions by setting  $m_t = m_d$  in equation (6) and varying  $\alpha$  between  $-10$  and  $10$ . The red star denotes the original solution  $m_d$  as shown in Figure 1. Note that the data misfit shown in Figure 2 is the data misfit for the full solution, i.e. including relocation parameters. By changing  $\alpha$ , we are able to

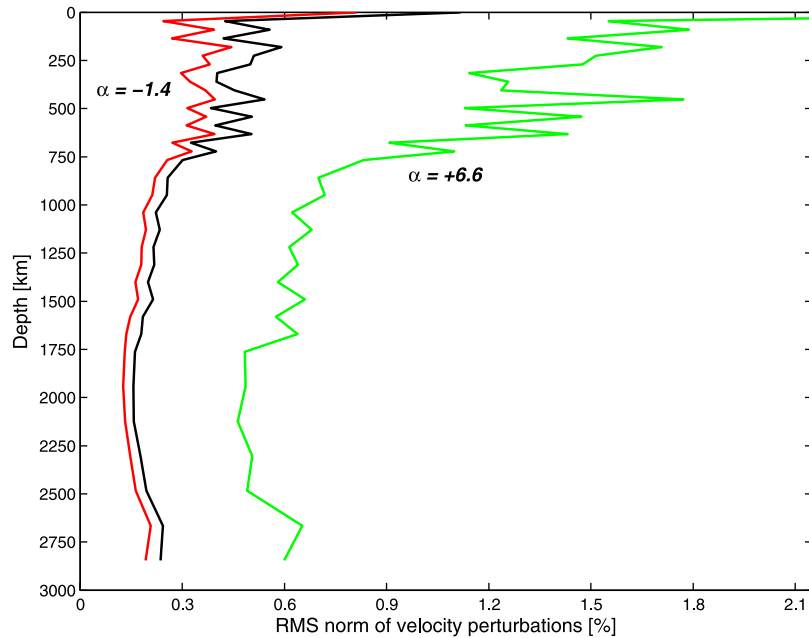


**Figure 3.** RMS norms of various solutions versus depth. Black line represents the original solution  $m_d$ . Red and green lines represent solutions for a  $\pm 0.1$  s change in RMS data misfit (see Figure 2).

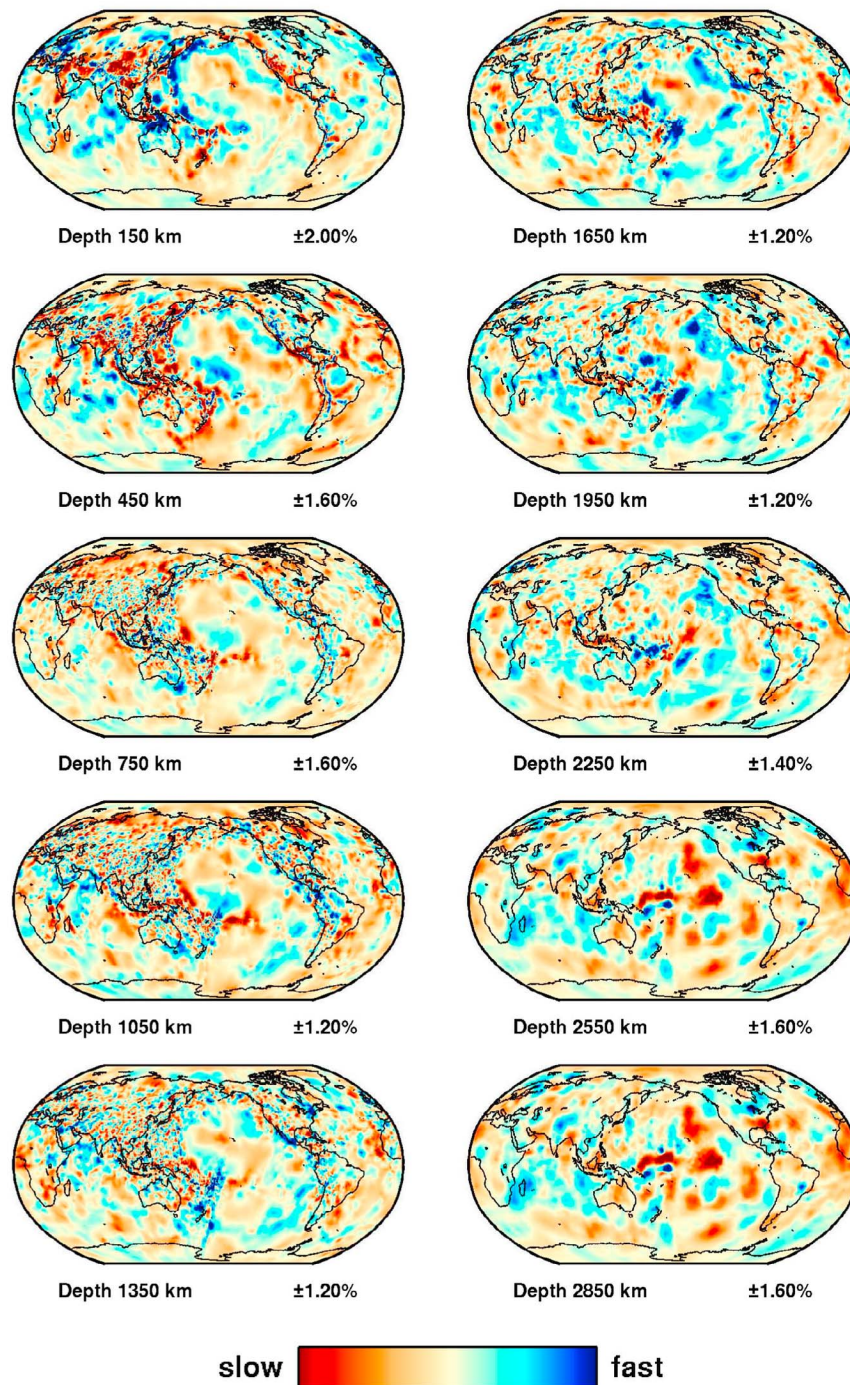


**Figure 4.** Difference between the extremes of the range of acceptable solutions given a tolerance of 0.1 s on the data misfit ( $\Delta m$  in Figure 2). These differences should be added to the minimum norm model in Figure 5 to obtain the maximum norm model for the 0.1 s tolerance level. Note that the color scale is different from that in Figure 1.

minimize the norm of the solution or improve the data misfit. Compared to the original solution the RMS norm is 24% smaller for  $\alpha = -1.7$ , for which the norm of the full solution reaches its minimum. The best data misfit is achieved for  $\alpha = 2.6$ . We find that the effect on the RMS data misfit of modifying the relocation parameters with the null-space shuttle is small compared to changing the slowness

parameters. A broad range of solutions exists that fits the data within a realistic average data uncertainty. As discussed above, we estimated the tolerance on the RMS data misfit for the current data set to be  $\pm 0.1$  s. For this tolerance, we find two intersection points with the range curve (Figure 2). The range in the model size is denoted by  $\Delta m$  and represents the set of acceptable solutions within the  $\pm 0.1$  s change in the

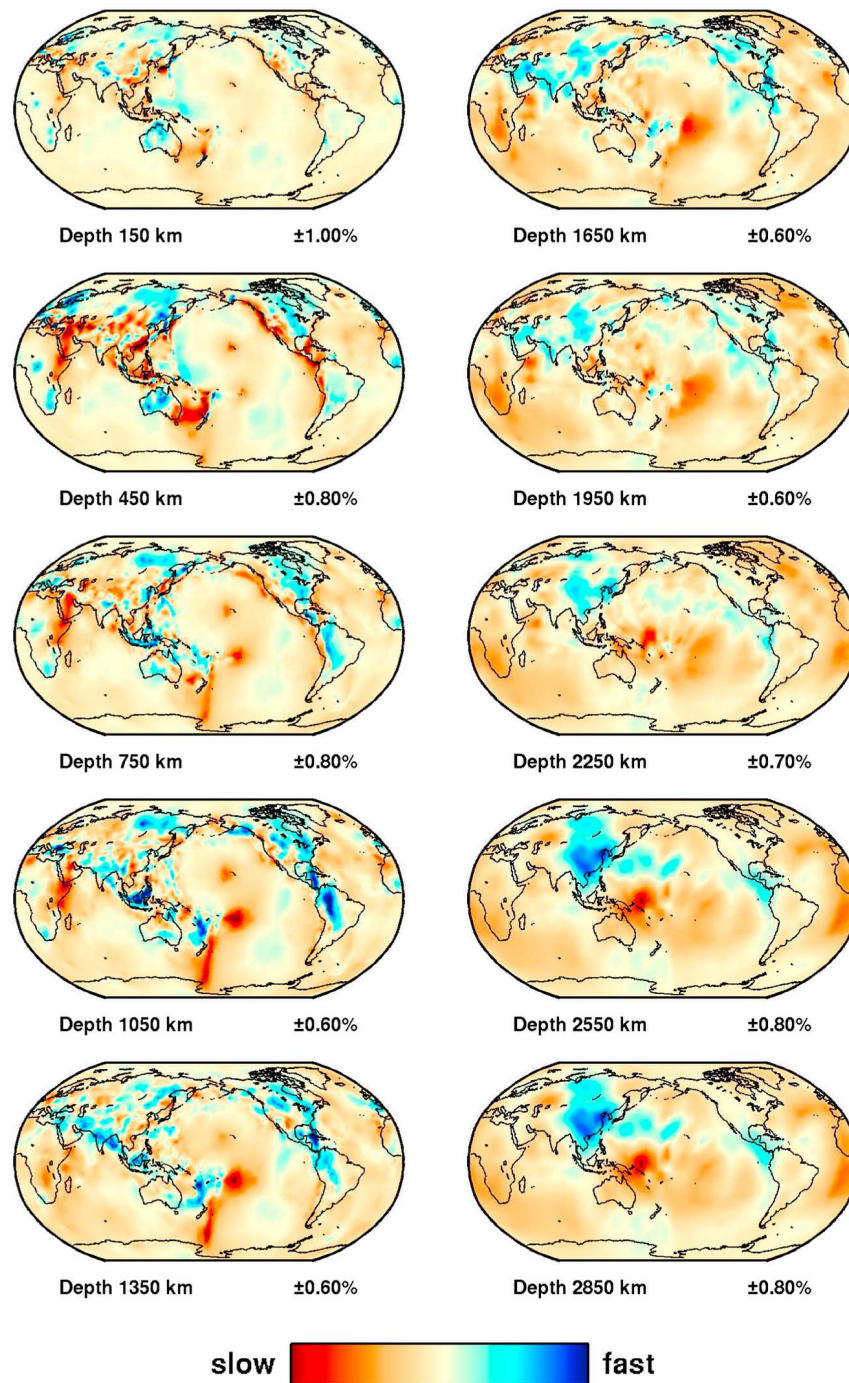


**Figure 5.** Approximate minimum norm model for  $\alpha = -1.4$ , corresponding to a data misfit tolerance of 0.1 s. The color scale is the same as in Figure 1.

RMS data misfit (bounded by  $\alpha = -1.4$  and  $\alpha = 6.6$ ). Clearly,  $\Delta m$  is very sensitive to the chosen data misfit tolerance. We show here the results for the 0.1 s tolerance level but discuss the dependency of  $\Delta m$  on data uncertainty below.

[20] To visualize the average behavior of the solution range, we translated that range into RMS velocity perturbations (excluding relocation parameters) versus depth (Figure 3) for the original solution (black curve) and the extreme bounds corresponding to  $\alpha = -1.4$  (red curve)

and  $\alpha = 6.6$  (green curve). In Figure 3, the maximum difference in average P-wave velocity perturbation is about 0.4% in the lower mantle and approximately 1% in the upper mantle at a depth of  $\sim 350$  km. Large uncertainties thus exist in the average RMS amplitude of the velocity perturbations. The difference between the models at the extreme ends of the solution range  $\Delta m$  is shown in Figure 4 and is of similar size to or larger than the amplitudes of anomalies in the original solution (Figure 1), particularly in

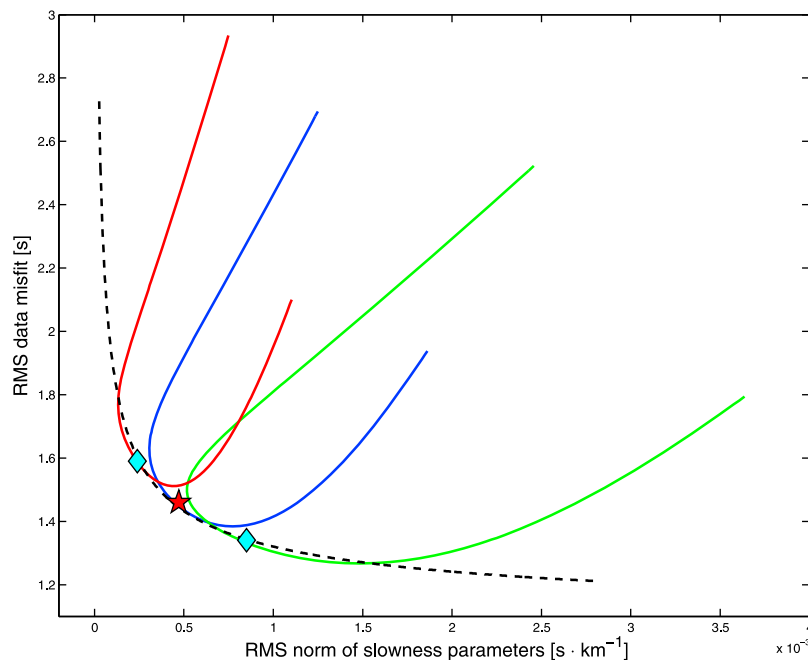


**Figure 6.** RMS data misfit of the tomographic solution versus RMS norm of slowness parameters for the original (blue curve), stronger (red) and weaker (green) regularization. A similar analysis as shown in Figure 2 was performed. Red star denotes the original solution  $m_d$ . Cyan diamonds represent the optimal solution for the chosen regularization. The black dashed line represents the classical L-curve analysis.

the upper mantle. Note that the color scale is different from that in Figure 1. By comparing Figures 1 and 4, we observe that most changes to the original model are made on relatively short length scales, i.e. a few hundred kilometers. This is an indication that the global model is not robust at those wavelengths.

[21] For the chosen tolerance on the data misfit of 0.1 s, the model in Figure 5 represents the model of velocity perturbations with the smallest norm required by the data (given the chosen regularization). It corresponds to the left intersection point between the green line and the blue curve in Figure 2, i.e. for  $\alpha = -1.4$ . The differences between this model (Figure 5) and the original model (Figure 1), in terms of geometry and amplitude of the velocity perturbations, are most pronounced in the upper mantle and in the Southern Hemisphere. Again we observe that, globally, the differences between the models are mainly for shorter wavelengths.

[22] The solution range estimated with the null-space shuttle depends on the particular regularization chosen for the tomographic inversion. Figure 6 shows the RMS data misfit versus the RMS norm of the slowness parameters in  $\tilde{m}^{new}$  for three different sets of values for the regularization parameters. As before, we apply equation (6) and use  $m_t = m_d$  and  $\alpha$  varying between  $-10$  and  $10$ . The blue curve represents the original regularization in Figure 2. As expected, an increase in the values of damping parameters results in a worse data fit and smaller model norm (red curve), while the opposite is true for a less strong regularization (green curve). The model range  $\Delta m$  clearly depends on the regularization via  $R$  (equation (7)). With the

regularization,  $\alpha$  changes as well for a fixed data misfit tolerance. We observe that  $\Delta m$  becomes larger for decreasing regularization, provided the inverse problem remains stable. The classical L-curve analysis to choose an optimal regularization corresponds to the tangent curve to the three range curves shown (Figure 6). We note that the optimal solution, that is, the solution to the inverse problem, is not the minimum norm solution. For a given regularization, we can always find a model with a smaller norm within the data misfit tolerance. As before, these null-space components mostly contain short wavelength structures.

## 5. Discussion

[23] This study does not provide a complete uncertainty analysis for tomographic models because we only sampled part of the model null-space. The approach is comparable to the extremal bound analysis of Meju [2009] for a fixed regularization. Whereas Meju's bounds are symmetric by construction and depend on the local misfit curvature, our bounds are not necessarily symmetric and depend on the null-space component of the model. The regularized tomographic inversion will include components of the model null-space in the final model due to the necessary trade-off between data misfit and regularization. These components can be removed from the model by using the null-space shuttle. As in Meju's approach, the null-space analysis depends on the chosen test model.

[24] For a data misfit tolerance of 0.1 s we found an approximate minimum norm model (Figure 5), which only contains structures required by the data. It is important to realize, however, that this minimum norm solution is not to

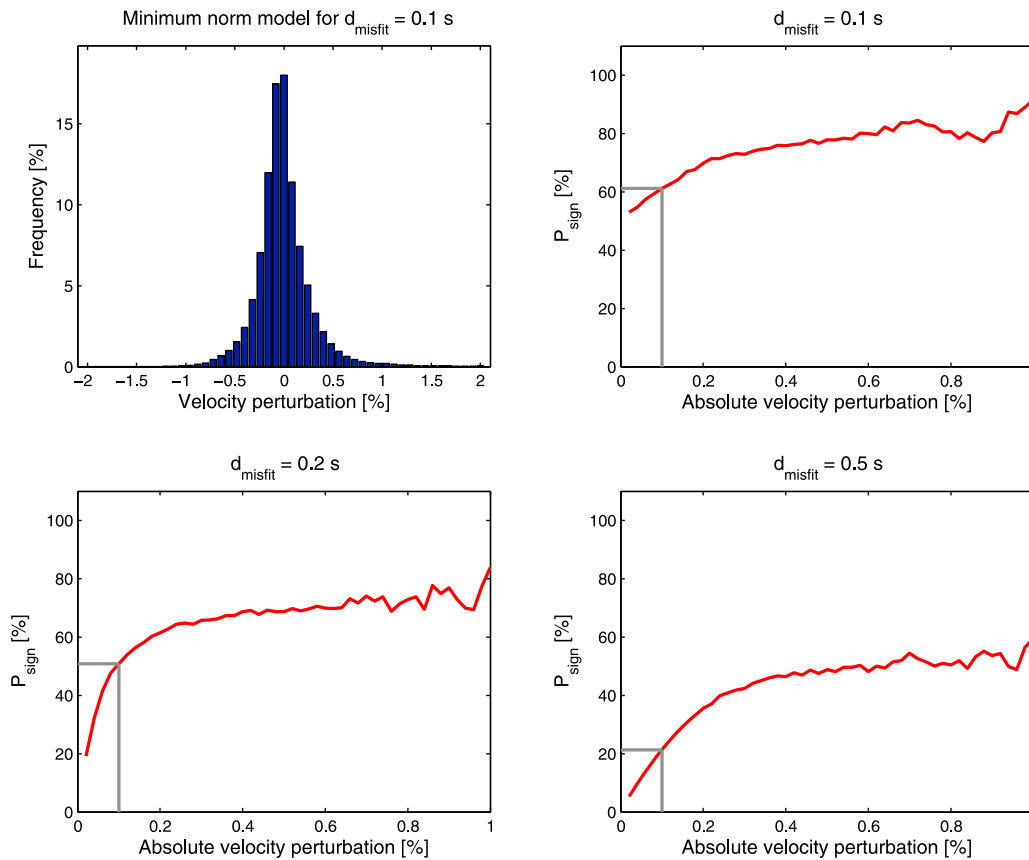


**Figure 7.** (top left) Histogram of velocity perturbations in the minimum norm model shown in Figure 5. (top right)  $P_{\text{sign}}$  versus absolute velocity perturbation for a data misfit tolerance of 0.1 s. Grey lines highlight  $P_{\text{sign}}$  for an absolute amplitude of 0.1% for the wave speed anomalies.  $P_{\text{sign}}$  for a tolerance of (bottom left) 0.2 s and (bottom right) 0.5 s.

be preferred over other solutions contained in  $\Delta m$  in Figure 2. We therefore suggest that tomographically inferred wave speed anomalies should be interpreted only if their sign is constrained by the data.

[25] We illustrate this concept for MIT-P08 and analyze the sign of the individual slowness parameters for all models in our set of acceptable solutions  $\Delta m$ . If a parameter does not have the same sign in all models, we consider it not to be constrained by the data, whereas a slowness parameter that has the same sign across the whole range  $\Delta m$  is considered to be robust. Figure 7 shows the histogram (Figure 7, top left) of the velocity perturbations in the minimum norm model (Figure 5). We show the percentage of model parameters for which the sign is constant across the range of acceptable solutions, which we call  $P_{\text{sign}}$ , for a data misfit tolerance of 0.1 s (Figure 7, top right). We show the results as a function of the absolute amplitude of the velocity perturbations in the minimum norm model. We find that the sign of  $\sim 65\%$  of all slowness parameters in the model is constrained for this data misfit level. We observe, not unexpectedly, that the sign is better constrained for model parameters which have a relatively high amplitude in the minimum norm model. For instance, for a data misfit level of 0.1 s the data constrain the sign of about 60% of the model parameters with an absolute amplitude of 0.1%. In

other words, 40% of the model parameters of 0.1% absolute amplitude are difficult to interpret since the sign of the wave speed anomalies is crucial for a solid interpretation. Model parameters with larger amplitudes in the minimum norm model are better constrained, e.g. 80% of the absolute velocity perturbations of 0.8% have an unchanged sign in the ensemble of solutions. We note that this simple analysis is based on averages over the global model and could be used to get a global sense of the constraint (or lack thereof) on the sign of individual model parameters. For the 0.1 s tolerance level, Figure 8 shows the model parameters for which the sign is robust over  $\Delta m$  in white, whereas unconstrained parameters are shown in grey. In accord with Figure 7, we observe that the majority of the slowness parameters is robust. In general, the unconstrained parameters correspond to the poorly sampled (oceanic) parts of the model. When the aim of a study is to interpret regional structures in the tomographic model, we recommend visually inspecting the robustness of the sign of the velocity perturbations (see below).

### 5.1. The Uncertainty of Data Uncertainty

[26] Uncertainties in the data are a crucial aspect in uncertainty analyses. True data uncertainty is generally not well known, and available estimates of the random and

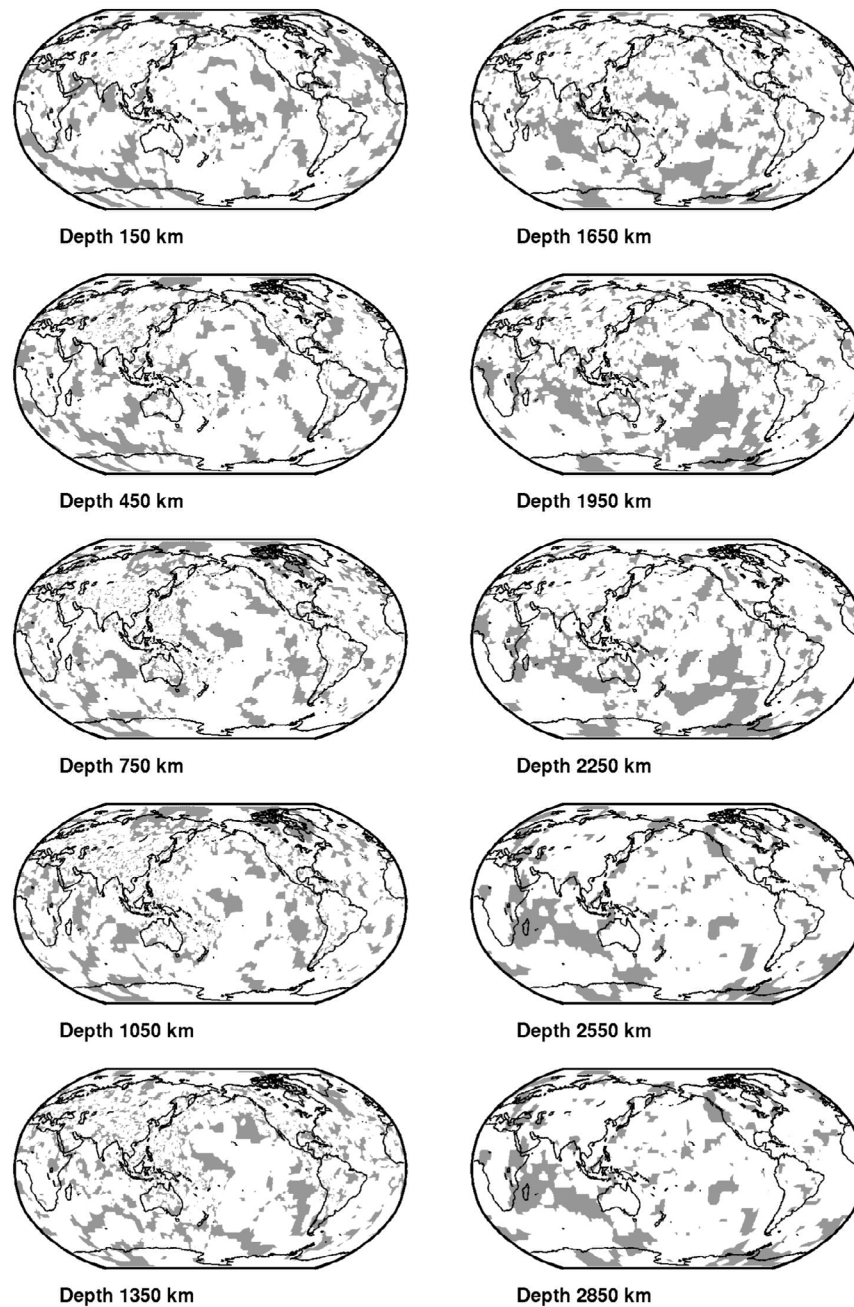


**Figure 8.** Model parameters for which the sign is constrained over  $\Delta m$  for a data misfit tolerance of 0.1 s. Constrained parameters are shown in white and unconstrained parameters in grey.

systematic errors in ISC data range from 0.5 s to 1.0 s. Since the tomographic models that we consider here use so-called composite rays, with typically 10 or more rays and associated travel time data combined into a single entry, we assume a smaller RMS data uncertainty. The analyses described above are based on an RMS error of +0.1 s, but this may underestimate the true data uncertainty (especially if the errors in the data are of a systematic nature [Röhm *et al.*, 1999]). Therefore, we also evaluated how the range of acceptable models,  $\Delta m$ , changes when we increase the RMS data uncertainty.

[27] When we increase the data misfit tolerance from 0.1 s to 0.2 s or even 0.5 s, the range of models, naturally, becomes broader. Note that for a tolerance of 0.5 s the extremes of the range will have approximately the same data misfit as the reference model *ak135* (1.92 s). The effect of the higher tolerance values is shown in Figure 7, where we show  $P_{sign}$  for presumed data uncertainties of 0.2 s (Figure 7, bottom left) and 0.5 s (Figure 7, bottom right). Note that for these larger data misfit tolerance levels, we use the corresponding minimum norm model, which is slightly different than for the 0.1 s level (see Figure 2). As expected,

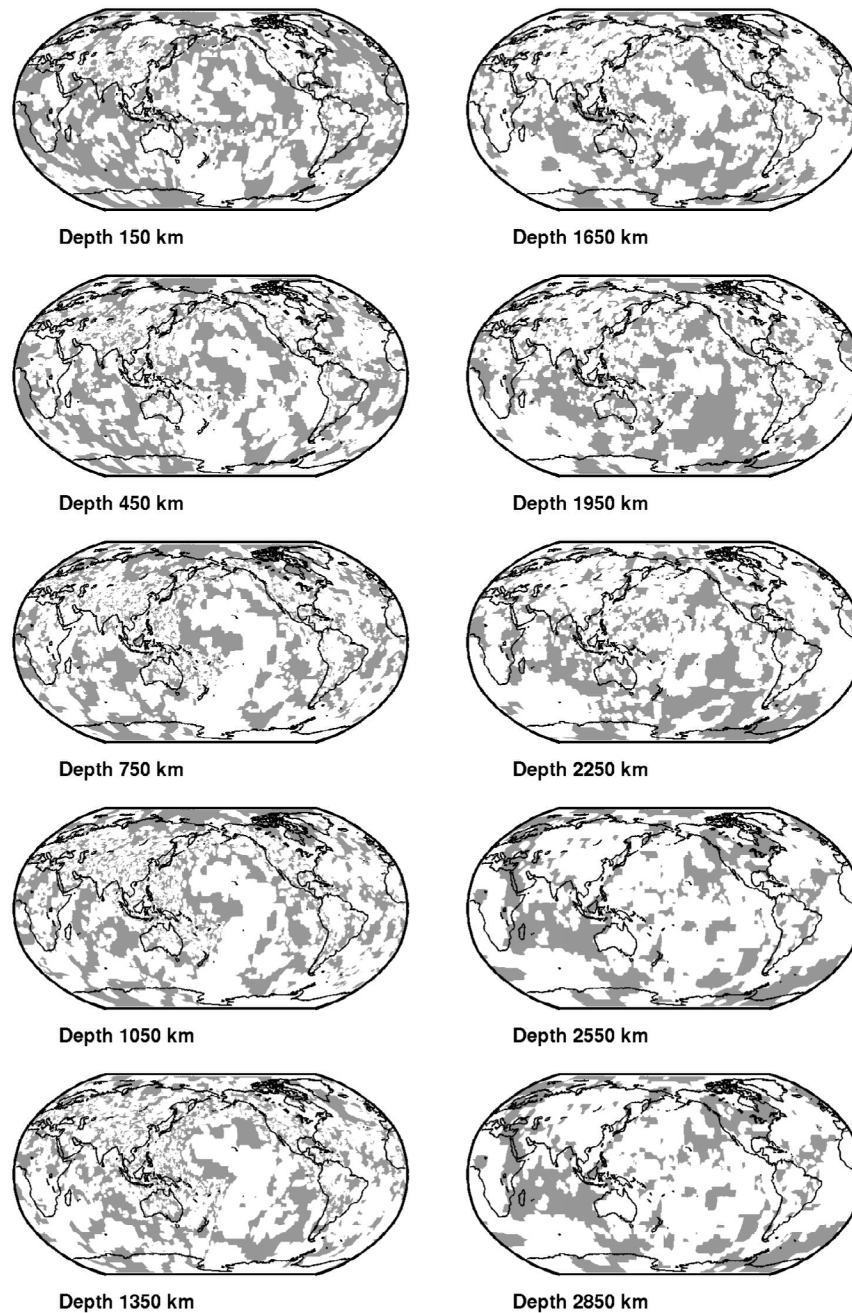


**Figure 9.** Model parameters for which the sign is constrained over  $\Delta m$  for a data misfit tolerance of 0.2 s. Constrained parameters are shown in white and unconstrained parameters in grey.

$P_{sign}$  decreases for these larger misfit tolerances, thus indicating a deteriorating constraint on the sign of wave speed anomalies (Figures 9 and 10).

## 5.2. Implication of Non-uniqueness of the Amplitude of Wave Speed Anomalies

[28] The non-uniqueness of the original solution is apparent in Figure 2. Whereas regularization is intended to reduce non-uniqueness by imposing *a priori* constraints, it is clear that for a given data misfit a broad range of viable solutions still exists. That the amplitudes of the anomalies

are so poorly constrained suggests that amplitudes in published tomographic models are dominated by the imposed regularization. Even if we can use the null-space shuttle to put quantitative bounds on the amplitude range, one should exercise much caution when making inferences based on amplitude. Consider, for instance, the estimation of thermochemical variations in Earth's lowermost mantle from tomographically inferred velocity perturbations. For illustration purposes, we take the two models represented by the red and green curve in Figure 3, which we denote as  $\tilde{m}_l$  (shown in Figure 5) and  $\tilde{m}_u$ , respectively. For a depth of

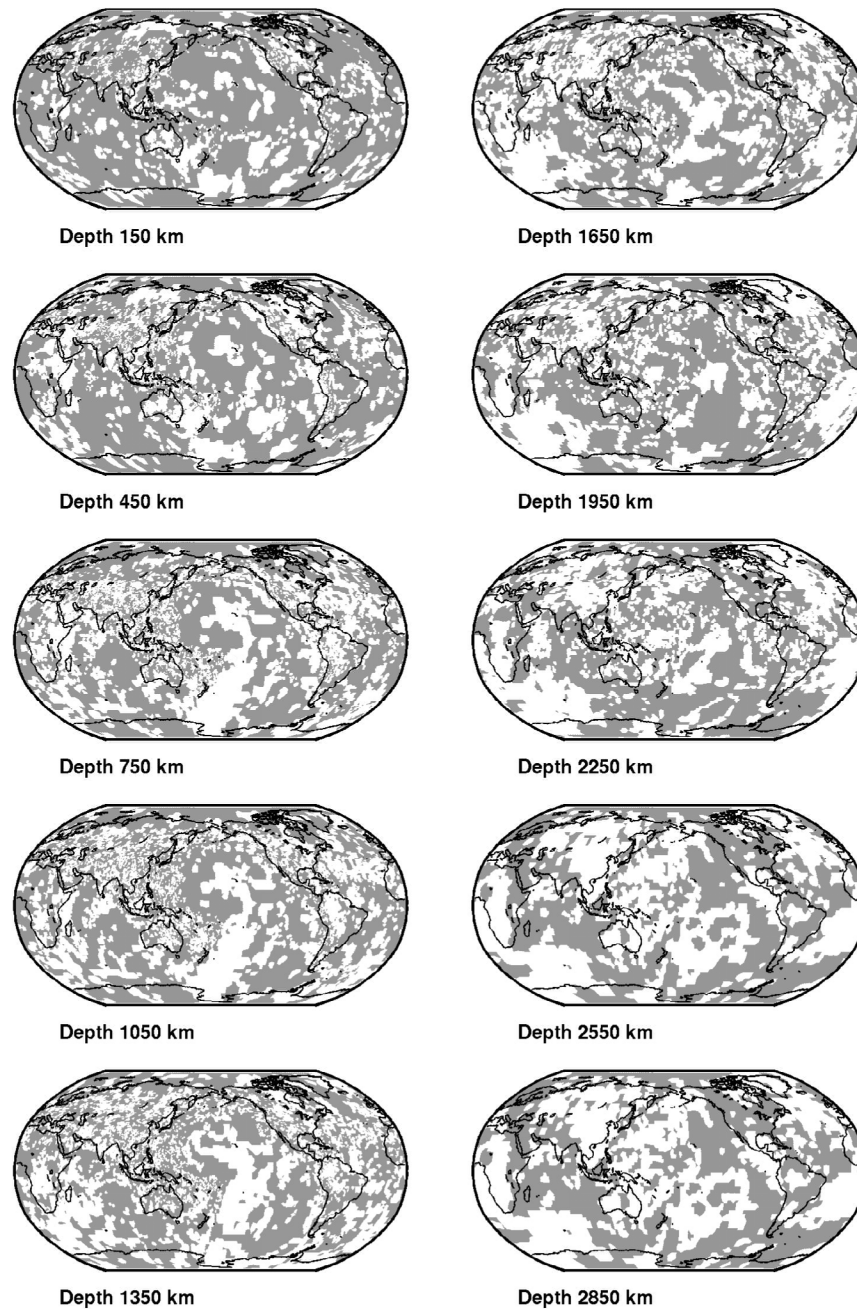


**Figure 10.** Model parameters for which the sign is constrained over  $\Delta m$  for a data misfit tolerance of 0.5 s. Constrained parameters are shown in white and unconstrained parameters in grey.

$\sim 2800$  km, we use a P-wave velocity to temperature sensitivity of  $\sim -1.6 \cdot 10^{-5}$  [Deschamps and Trampert, 2003]. At this depth, model  $\tilde{m}_l$  would yield a temperature range from  $-400$  to  $+500$  K (with an RMS of  $\sim 120$  K). At the same depth, model  $\tilde{m}_u$ , which is also acceptable by the seismological data used, would yield a temperature range from  $-2000$  to  $+2500$  K (with an RMS of  $\sim 375$  K). The temperature range inferred from  $\tilde{m}_l$  may seem plausible, and may suggest that the velocity perturbations in the lowermost mantle have a purely thermal origin. By contrast, the use of model  $\tilde{m}_u$  could lead to the conclusion that factors other than

temperature (such as variations in bulk composition) are needed to explain wave speed variations in the lowermost mantle. These models could thus be used in support of fundamentally different views on thermochemical variations, but the differences are not constrained by data but by null-space components.

[29] Interpretations based on absolute values of the magnitude of tomographically inferred wave speed anomalies should thus be evaluated with this uncertainty in mind. We note that relative variations in P and S wave speeds – expressed, for instance, as wave speed or Poisson’s ratios–

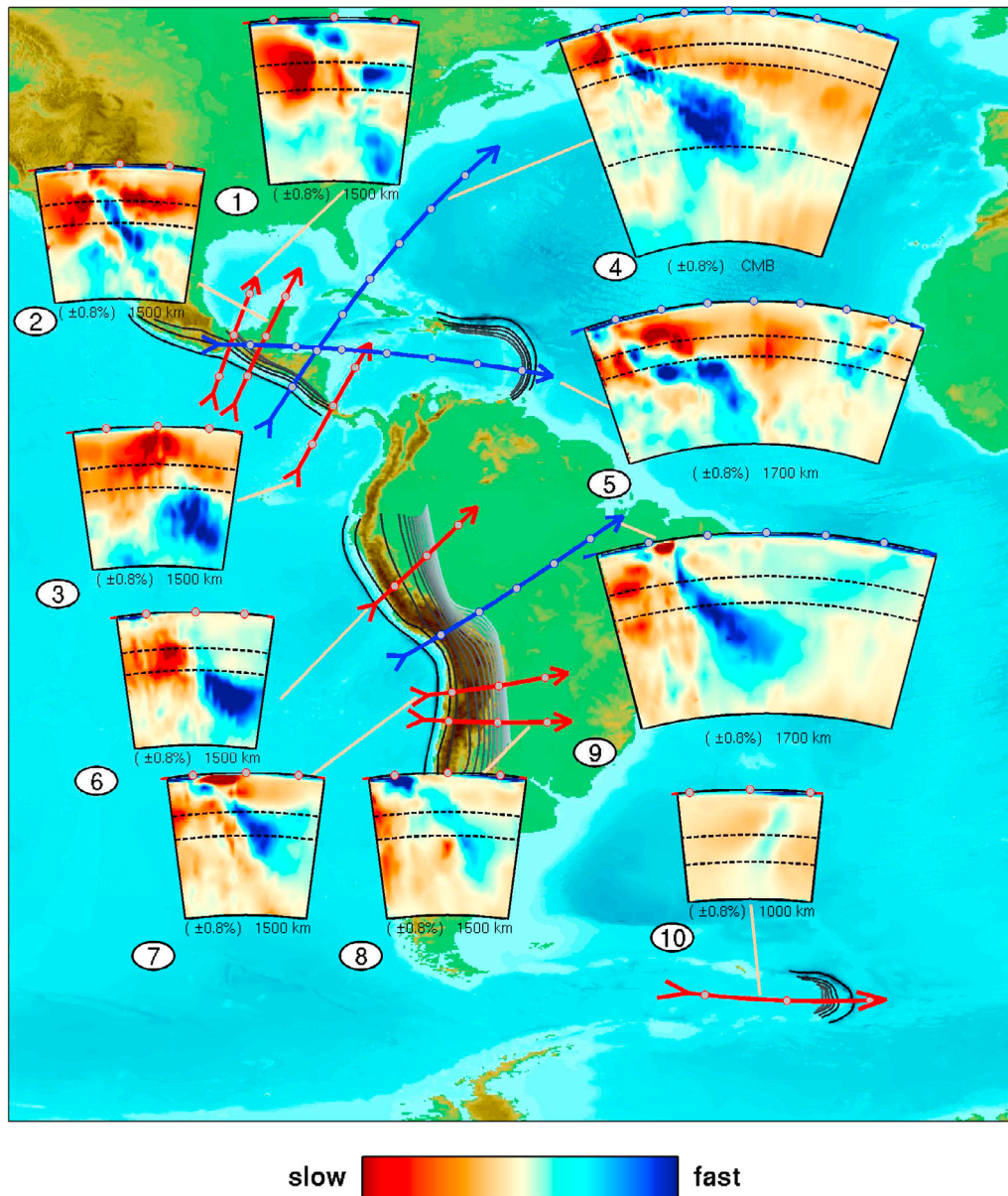


**Figure 11.** Original model  $m_d$  for the South American region. The color scale ranges from  $-0.8$  to  $+0.8\%$ .

can produce a more robust diagnostic for compositional heterogeneity [Trampert and van der Hilst, 2005], and this has indeed been more commonly used [e.g., Su and Dziewonski, 1997; Kennett et al., 1998; Saltzer et al., 2001, 2004] than absolute wave speed perturbations.

### 5.3. Robustness of Small Scale Structure

[30] An important, but not unexpected, result is that (on a global scale) the null-space components in the original model (Figure 1) mostly concern shorter wavelength structures (cf. Figures 4 and 5). This suggests that model parameters are not constrained robustly everywhere at the scale of the block parameterization ( $<200$  km), and that in many regions small scale structure is poorly resolved and highly sensitive to data noise and regularization.

[31] Obviously, this does not mean that this small scale structure is not there, nor does it rule out that in the better sampled regions such small scale structure is resolved by the data used. But it does mean that this structure should be interpreted with considerable caution and, preferably, only in combination with independent observations and constraints (e.g. seismicity, volcanism, gravity anomalies and regional geologic and tectonic histories). This should be borne in mind when using small scale structure in interpretations concerning physical processes such as downwelling of slabs, upwelling of mantle plumes and, ultimately, mantle convection. We recommend that interpretations relying solely on tomography should be restricted to structures in the minimum norm model for which the sign of the wave speed anomaly is constrained by the data.

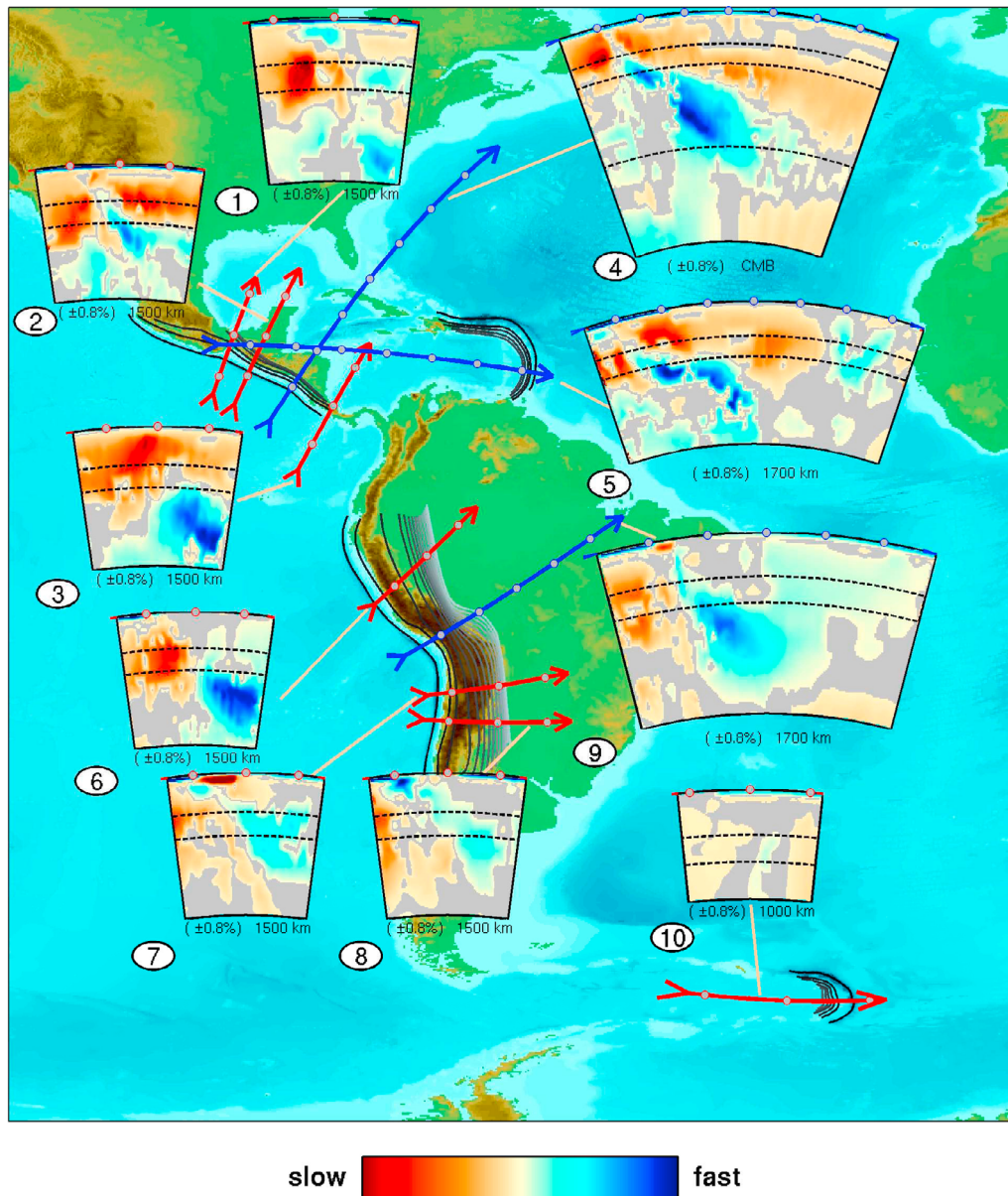


**Figure 12.** Approximate minimum norm model for a data misfit tolerance of 0.1 s for the South American region. Model parameters for which the sign is not constrained over  $\Delta m$  are set to zero and shown in grey. The color scale ranges from  $-0.8$  to  $+0.8\%$ .

#### 5.4. Robustness of Deep Subduction and Mantle Plumes

[32] In the context of mantle convection, it is important to know if the tomographic images of deep slabs (that is, beyond the parts that can be considered as known to exist from Wadati-Benioff seismicity) and low-velocity (plume-like) structures are robust (that is, required by the data) or whether they are artefacts due to a combination of preferred sampling and regularization. This has been investigated qualitatively using test inversions with synthetic data [e.g., Spakman *et al.*, 1989; van der Hilst, 1995; Li *et al.*, 2008], but we can also use the method presented here to investigate if pertinent parts of the slab and plume images are required

by the data. To do so, we suggest to visualize the original solution (Figure 1) together with the part of the minimum norm solution that has a constant sign across the solution range  $\Delta m$ . We show examples for a data misfit tolerance of 0.1 s, 0.2 s and 0.5 s and set all slowness parameters to zero for which the sign is not constrained over  $\Delta m$ . This enables us to visualize which part of the structures is constrained in by the data and can thus be interpreted as robust.

##### 5.4.1. Deep Slabs

[33] For the subduction systems that are most often presented as examples where slabs of subducted lithosphere sink into the lower mantle, for example, the Americas, Indonesia, Tonga, it appears that it is not possible to project the pertinent

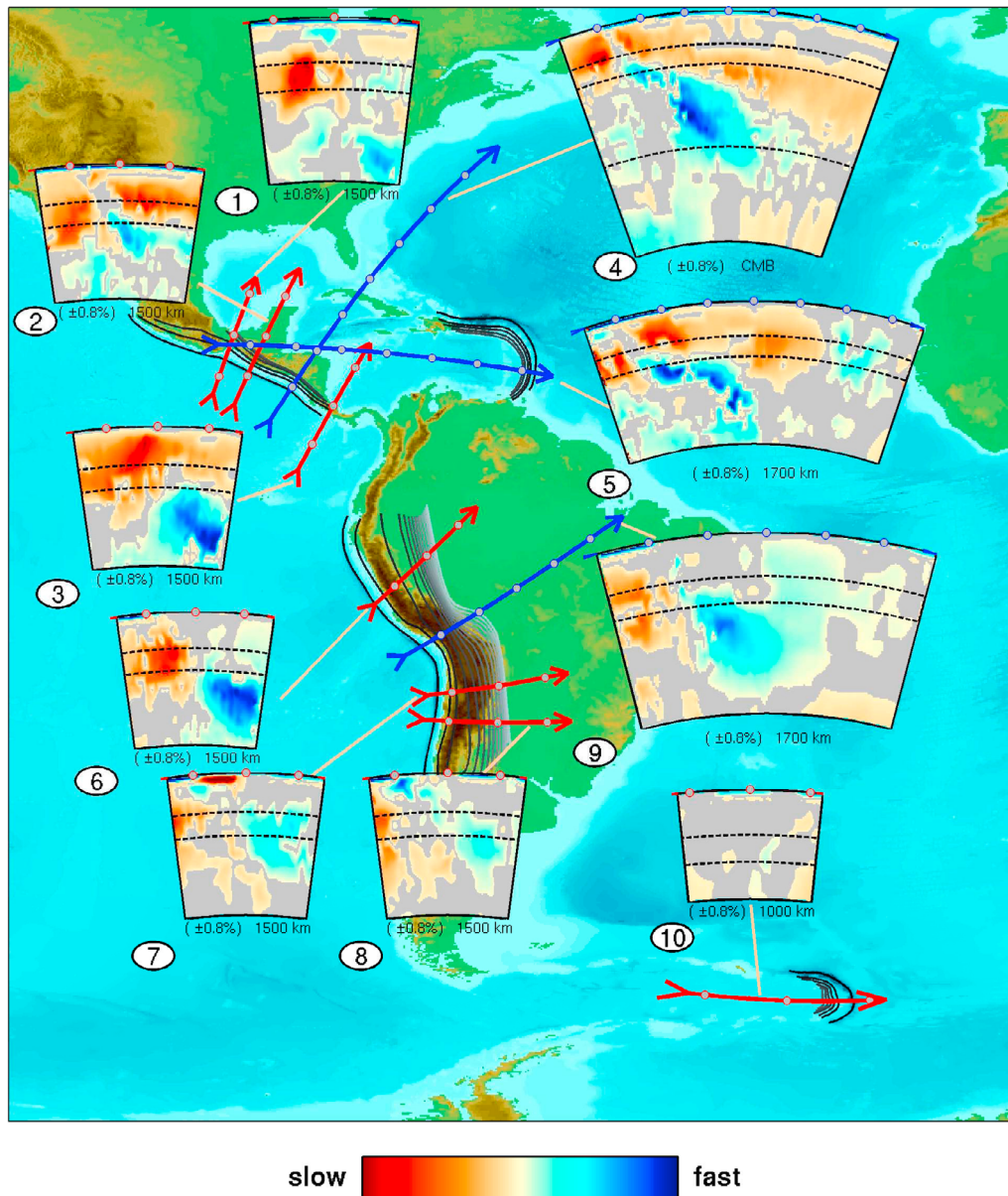


**Figure 13.** Approximate minimum norm model for a data misfit tolerance of 0.2 s for the South American region. Model parameters for which the sign is not constrained over  $\Delta m$  are set to zero and shown in grey. The color scale ranges from  $-0.8$  to  $+0.8\%$ .

structures onto the model null-space. Figures 11–14 illustrate this for the slab systems beneath Central and South America. An important first-order inference is that the deep slabs imaged in the original tomographic model (Figure 11) are also present in the approximate minimum norm model and pass our constant sign robustness criterion, even for data misfit tolerances up to 0.5 s (Figures 12–14). From such analyses we conclude that the high wave speed anomalies that are often interpreted as lower mantle parts of the slabs are indeed required by the travel time data used, thus justifying interpretations in terms of plate reconstructions and deep subduction [e.g., Grand, 1994; Grand et al., 1997; van der Hilst et al., 1997; Bijwaard et al., 1998; Replumaz et al., 2004; Ren et al., 2007]. Owing to more limited sampling,

the narrow upper mantle parts of the downgoing slab are often not as well resolved as the deeper parts, but the presence of slabs of subducted oceanic lithosphere in the upper mantle is uncontroversial since they are well constrained by, for instance, seismicity and volcanism. Other parts of presumed subducted slabs that are generally poorly resolved by travel time data are the subhorizontal structures in the transition zone, often referred to as stagnant slabs [van der Hilst et al., 1991; Fukao et al., 1992, 2001]. The presence of these structures is supported, however, by multimode surface wave studies [e.g., Fukao et al., 2001; Lebedev and Nolet, 2003; Ritsema et al., 2004] and the regional geology and the tectonic histories of the slab systems involved [e.g., van der Hilst and Seno,

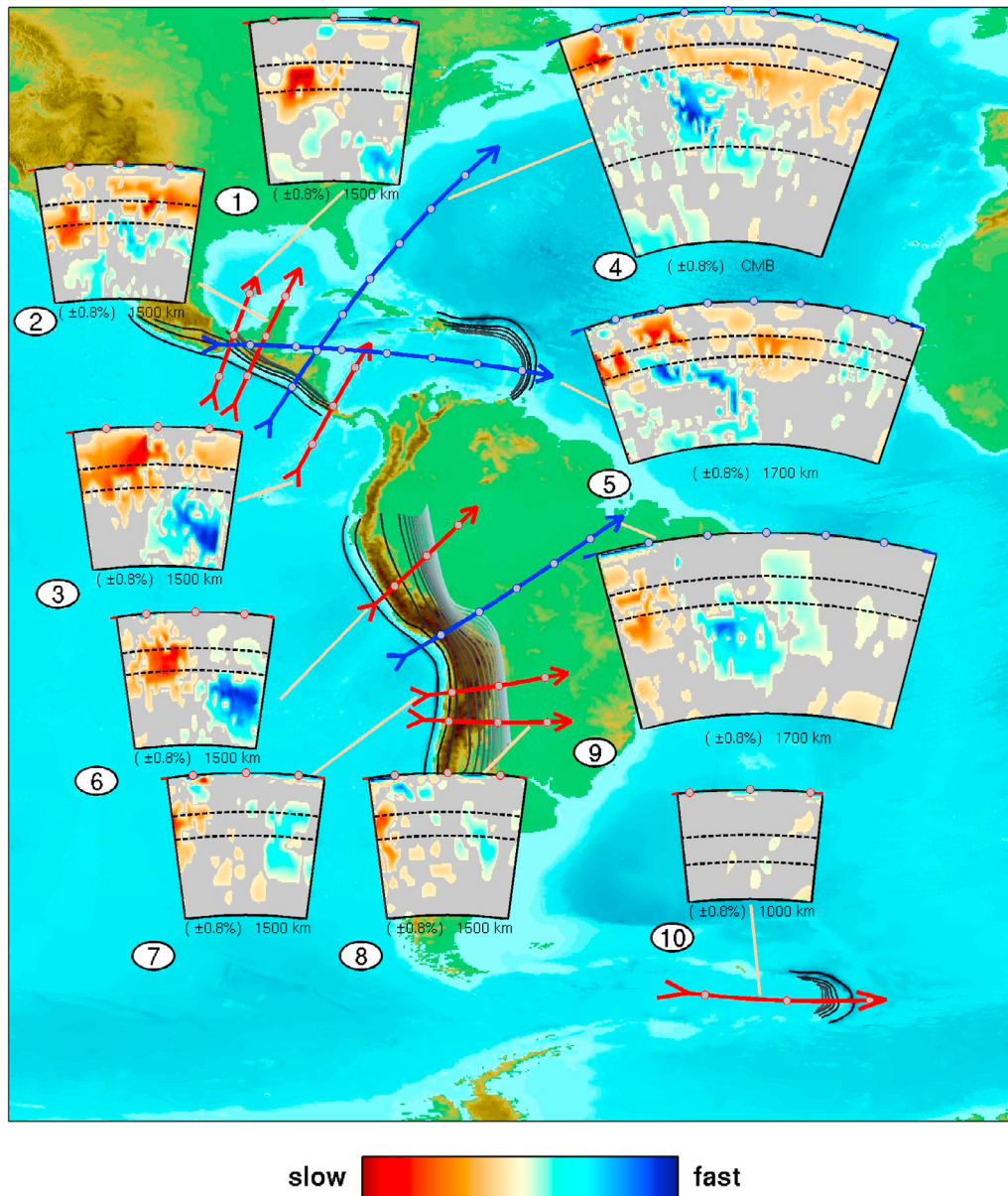


**Figure 14.** Approximate minimum norm model for a data misfit tolerance of 0.5 s for the South American region. Model parameters for which the sign is not constrained over  $\Delta m$  are set to zero and shown in grey. The color scale ranges from  $-0.8$  to  $+0.8\%$ .

1993; Griffiths *et al.*, 1995; Bijwaard *et al.*, 1998; Huang and Zhao, 2006].

#### 5.4.2. Mantle Plumes

[34] We find that the slow anomalies that are often interpreted as upwellings of mantle plumes, for instance underneath Hawaii, Iceland, Africa [e.g., Bijwaard and Spakman, 1999; Montelli *et al.*, 2004; Wolfe *et al.*, 2009], show a varying degree of robustness. As an example we show for MIT-P08 the tomographically inferred wave speed anomalies beneath Iceland (Figure 15) and Hawaii (Figure 16). Figures 15 and 16 show the original model and the approximate minimum norm model in  $\Delta m$  for data misfit tolerances of 0.1 s, 0.2 s and 0.5 s. Again, the parameters in the minimum norm model for which the sign is not constrained over

$\Delta m$  are set to zero. Whether the low-velocity structure beneath Iceland is constrained in sign depends very much on the data misfit tolerance (Figure 15). In MIT-P08 the shape of the anomaly is not robust and we observe a clear difference between the original model and the narrow low-amplitude low-velocity structure in the minimum norm model. Similar (visual) analysis suggests that mantle structure beneath Hawaii (Figure 16) is more robust than below Iceland. The presence of anomalously low P-wave speeds in the upper mantle and transition zone west of Hawaii, that is, in the same region where Cao *et al.* [2011] inferred high transition zone temperatures from images of interface topography, seems required by the data used in the construction of MIT-P08. However, the depth extent of the low

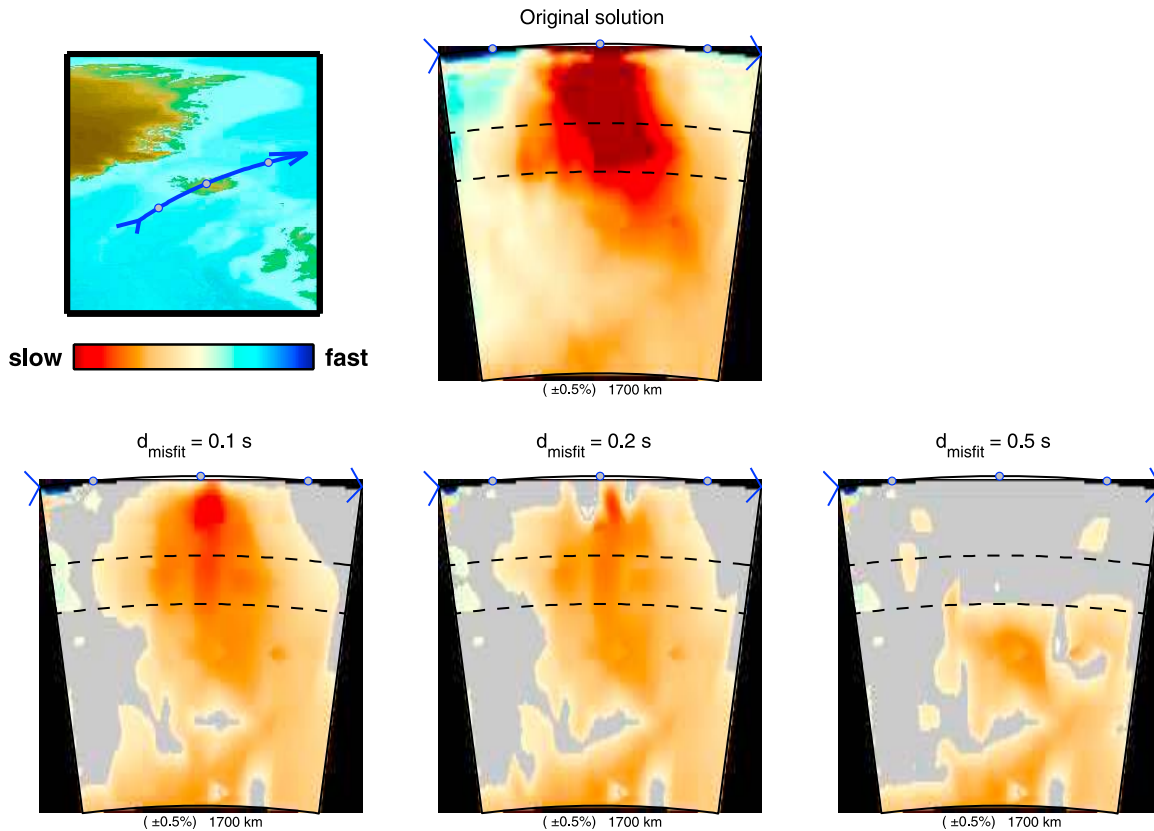


**Figure 15.** (top) Original model and the approximate minimum norm model for a data misfit tolerance of (bottom left) 0.1 s, (bottom middle) 0.2 s, and (bottom right) 0.5 s beneath Iceland. Model parameters for which the sign is not constrained over  $\Delta m$  are set to zero and shown in grey. The color scale ranges from  $-0.5$  to  $+0.5\%$ .

velocity anomaly, that is, its possible continuation into the lowermost mantle (toward the core-mantle boundary), is not constrained by the data used in MIT-P08.

[35] We reiterate that these observations do not by themselves refute hypotheses on the existence and depth extent of (upwellings of) mantle plumes. It simply indicates that even though travel time data require low-velocity structures in these mantle regions, they can not yet constrain their shape and depth extent. Plume-like structures in tomographic models such as MIT-P08 should, thus, be interpreted with caution and preferably in conjunction with independent observations.

## 6. Summary and Conclusions

[36] Whether or not tomographically inferred anomalies are robust, that is, required by the data, is important from a physical point of view, since they help shape our understanding of physical processes such as downwelling of slabs, upwelling of mantle plumes and, ultimately, mantle convection. Since the advent of seismic tomography over three decades ago, researchers have focused on improving spatial resolution, benefitting from ever increasing computational power and data quantity and quality, but relatively little attention is being paid to the quality and (fundamental) non-uniqueness of the images.

[37] As an alternative to sensitivity tests with synthetic data, we propose to explore the model null-space to identify acceptable solutions of linearized tomographic inversions. The range of acceptable models depends on a predefined tolerance on the data misfit and regularization. Besides being straightforward to implement, the method allows one to find new solutions that can be easily visualized and interpreted in a physical sense, similar to the representation of the original solution. We illustrated these concepts for one tomographic model (MIT-P08) but stress that the conclusions are relevant for all similar such models.

[38] Tomographic models are notoriously non-unique and substantial parts of the original models can lie in the null-space of the forward operator (Figure 2). Using the null-space shuttle [Deal and Nolet, 1996], one can quantitatively evaluate the range of solutions ( $\Delta m$ ) that satisfy the tomographic data, and we suggest to consider  $\Delta m$  when interpreting structures based solely on tomography. As a practical measure of robustness, we propose to use the stability of the sign of a particular model parameter. If its value is not consistently positive or negative over  $\Delta m$ , then the parameter is not uniquely constrained by the data. This is most pertinent for velocity perturbations of low amplitude ( $<0.2\%$ ) and sign stability decreases with increasing data misfit tolerance (Figures 7–10).

[39] For a conservative change in RMS data misfit of  $\pm 0.1$  s, we find a broad range of solutions that are

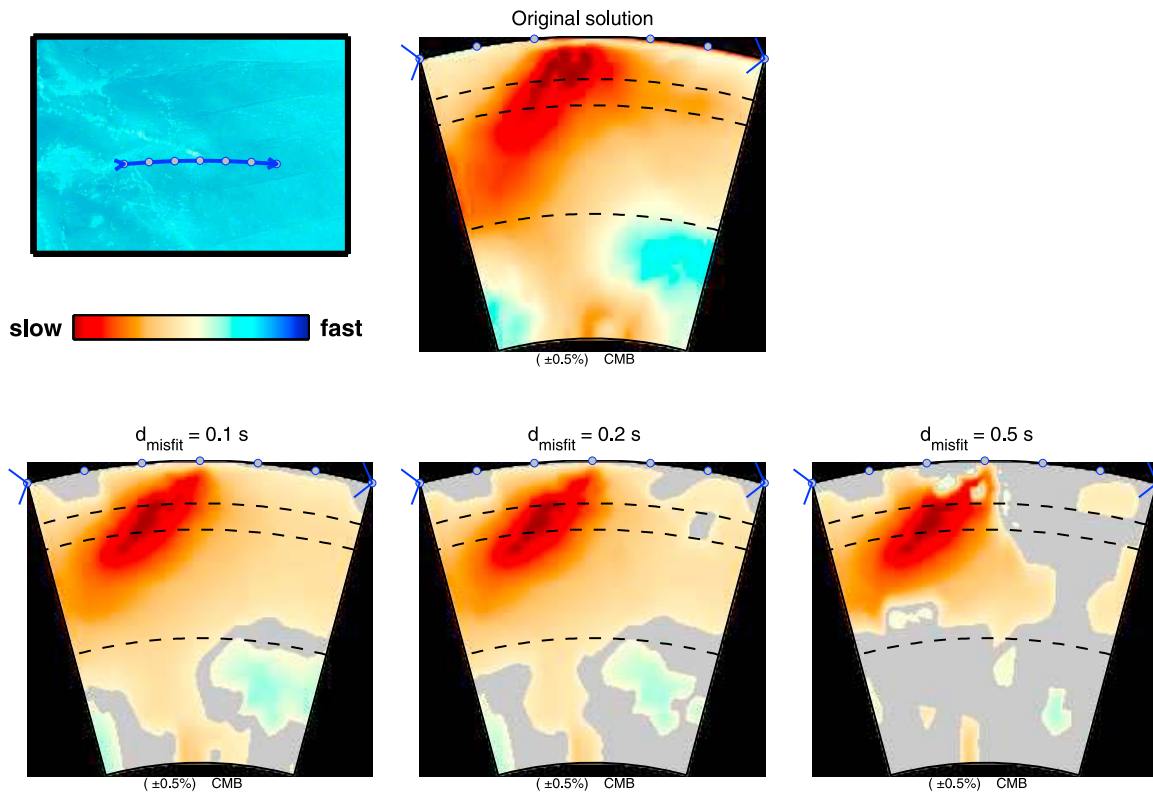


**Figure 16.** (top) Original model and the approximate minimum norm model for a data misfit tolerance of (bottom left) 0.1 s, (bottom middle) 0.2 s, and (bottom right) 0.5 s beneath Hawaii. Model parameters for which the sign is not constrained over  $\Delta m$  are set to zero and shown in grey. The color scale ranges from  $-0.5$  to  $+0.5\%$ .

compatible with the travel time data used for global tomography by *Li et al.* [2008]. For test models with a similar data misfit (given the tolerance) as the original solution, MIT-P08, the RMS velocity perturbations vary from 0.2 to 0.6% in the lowermost mantle and from 0.3 to 1.3% in the upper mantle (Figure 3). Such large variations in average amplitudes prohibit robust inferences on thermochemical variations in the Earth solely from tomographic models (based on currently available travel time residuals).

[40] Independent of regularization we find that on a global scale much of the short wavelength variations resides in the model null-space, suggesting that the data do not everywhere resolve structure on the smallest length scale ( $<200$  km) allowed by the (block) parameterization used in MIT-P08 and similar models. This does not mean that such structure does not exist or that such structure is not constrained in well sampled areas. But it does mean that such structure is in general not robust and should be interpreted with great care, preferably along with independent information from other sources, such as geological studies, plate reconstructions, the geometry of Wadati-Benioff zones, and geodynamical modeling, as has been done in many global [e.g., *van der Hilst et al.*, 1997; *Grand et al.*, 1997; *Bunge and Grand*, 2000] and regional [e.g., *van der Hilst and Seno*, 1993; *van der Hilst*, 1995; *van der Voo et al.*, 1999; *Replumaz et al.*, 2004; *Miller et al.*, 2006] studies.

[41] Application of the null-space shuttle shows that the high velocity anomalies in the lower mantle, which are often interpreted as evidence for slab penetration into the lower

mantle [e.g., *Richards and Engebretson*, 1992; *Ricard et al.*, 1993; *van der Hilst et al.*, 1997; *Grand et al.*, 1997], are robust in that they are required by the seismic data. Low-velocity anomalies that are commonly interpreted as (upwellings of) mantle plumes, for instance underneath Hawaii, Iceland and Africa, show varying degrees of robustness. In general, the travel time data do require a low-velocity structure, but the shape and depth extent of such plume-like anomalies is not fully constrained in every region by travel time data alone. Indeed, as was noted by *Li et al.* [2008], to resolve present-day controversies about ‘plume imaging’ requires a dramatic improvement in data coverage, especially in oceanic regions. The conjunction of various types of seismic data and other independent observations, improved data coverage (in particular in oceanic regions), as well as the improvement of both forward and inverse methods, will help to overcome these controversies in the future.

[42] **Acknowledgments.** We thank Jeroen Ritsema and an anonymous referee for constructive reviews. Computational resources for this work were provided by the Netherlands Research Center for Integrated Solid Earth Science (ISES 3.2.5 High End Scientific Computation Resources).

## References

Aki, K., A. Christofferson, and E. S. Husebye (1977), Determination of the three-dimensional seismic structure of the lithosphere, *J. Geophys. Res.*, *82*, 277–296.

- Amaru, M. L., W. Spakman, A. A. Villaseñor, S. Sandoval, and E. Kissling (2008), A new absolute arrival time data set for Europe, *Geophys. J. Int.*, *173*, 465–472.
- Bijwaard, H., and W. Spakman (1999), Tomographic evidence for a narrow whole mantle plume below Iceland, *Earth Planet. Res. Lett.*, *166*, 121–126.
- Bijwaard, H., and W. Spakman (2000), Non-linear global P-wave tomography by iterated linearized inversion, *Geophys. J. Int.*, *141*, 71–82.
- Bijwaard, H., W. Spakman, and E. R. Engdahl (1998), Closing the gap between regional and global travel time tomography, *J. Geophys. Res.*, *103*, 30,055–30,078.
- Boschi, L. (2003), Measures of resolution in global body wave tomography, *Geophys. Res. Lett.*, *30*(19), 1978, doi:10.1029/2003GL018222.
- Bunge, H. P., and S. P. Grand (2000), Mesozoic plate-motion history below the northeast Pacific Ocean from seismic images of the subducted Farallon slab, *Nature*, *405*, 337–340.
- Cao, Q., R. D. van der Hilst, M. V. de Hoop, and S.-H. Shim (2011), Seismic imaging of transition zone discontinuities suggests hot mantle west of Hawaii, *Science*, *332*, 1068–1071.
- Deal, M. M., and G. Nolet (1996), Nullspace shuttles, *Geophys. J. Int.*, *124*, 372–380.
- Deal, M. M., G. Nolet, and R. D. van der Hilst (1999), Slab temperature and thickness from seismic tomography: 1. Method and application to Tonga, *J. Geophys. Res.*, *104*(B12), 28,789–28,802, doi:10.1029/1999JB900255.
- Deschamps, F., and J. Trampert (2003), Mantle tomography and its relation to temperature and composition, *Phys. Earth Planet. Inter.*, *140*, 277–291.
- Dziewonski, A. M., B. H. Hager, and R. J. O'Connell (1977), Large-scale heterogeneities in the lower mantle, *J. Geophys. Res.*, *82*, 239–255.
- Engdahl, E. R., R. D. van der Hilst, and R. Buland (1998), Global teleseismic earthquake relocation with improved travel times and procedures for depth determination, *Bull. Seismol. Soc. Am.*, *88*, 722–743.
- Fukao, Y., M. Obayashi, H. Inoue, and M. Nishii (1992), Subducting slabs stagnant in the mantle transition zone, *J. Geophys. Res.*, *97*, 4809–4822.
- Fukao, Y., S. Widiyantoro, and M. Obayashi (2001), Stagnant slabs in the upper and lower mantle transition zone, *Rev. Geophys.*, *39*, 291–323.
- Grand, S. P. (1990), A possible station bias in travel time measurements reported to ISC, *Geophys. Res. Lett.*, *17*(1), 17–20.
- Grand, S. P. (1994), Mantle shear structure beneath the Americas and surrounding oceans, *J. Geophys. Res.*, *99*, 11,591–11,621, doi:10.1029/94JB00042.
- Grand, S. P. (2002), Mantle shear-wave tomography and the fate of subducted slabs, *Philos. Trans. R. Soc. London*, *360*, 2475–2491.
- Grand, S. P., R. D. van der Hilst, and S. Widiyantoro (1997), Global seismic tomography: A snapshot of convection in the Earth, *GSA Today*, *7*(4), 1–7.
- Griffiths, R. W., R. Hackney, and R. D. van der Hilst (1995), A laboratory investigation of effects of trench migration on the descent of subducted slabs, *Earth Planet. Sci. Lett.*, *133*, 1–17.
- Gudmundsson, O., J. H. Davies, and R. W. Clayton (1990), Stochastic analysis of global traveltimes data: Mantle heterogeneity and random errors in the ISC data, *Geophys. J. Int.*, *102*, 24–43.
- Huang, J., and D. Zhao (2006), High resolution mantle tomography of China and surrounding regions, *J. Geophys. Res.*, *111*, B09305, doi:10.1029/2005JB004066.
- Kárason, H., and R. D. van der Hilst (2000), Constraints on mantle convection from seismic tomography, in *History and Dynamics of Plate Motion*, *Geophys. Monogr. Ser.*, vol. 121, pp. 277–288, edited by M. A. Richards, R. Gordon, and R. D. van der Hilst, AGU, Washington, D. C.
- Kárason, H., and R. D. van der Hilst (2001), Tomographic imaging of the lowermost mantle with differential times of refracted and diffracted core phases (PKP,  $P_{diff}$ ), *J. Geophys. Res.*, *106*, 6569–6588.
- Kennett, B. L. N., E. R. Engdahl, and R. Buland (1995), Constraints on seismic velocities in the Earth from travel times, *Geophys. J. Int.*, *122*, 108–124.
- Kennett, B. L. N., S. Widiyantoro, and R. D. van der Hilst (1998), Joint seismic tomography for bulk-sound and shear wavespeed, *J. Geophys. Res.*, *103*, 12,469–12,493.
- Lebedev, S., and G. Nolet (2003), Upper mantle beneath Southeast Asia from *S* velocity tomography, *J. Geophys. Res.*, *108*(B1), 2048, doi:10.1029/2000JB000073.
- Lévêque, J. J., L. Rivera, and G. Wittlinger (1993), On the use of the checker-board test to assess the resolution of tomographic inversions, *Geophys. J. Int.*, *115*, 313–318.
- Li, C., R. D. van der Hilst, E. R. Engdahl, and S. Burdick (2008), A new global model for *P* wave speed variations in Earth's mantle, *Geochem. Geophys. Geosyst.*, *9*, Q05018, doi:10.1029/2007GC001806.
- Meju, M. A. (2009), Regularized extremal bounds analysis (REBA): An approach to quantifying uncertainty in nonlinear geophysical inverse problems, *Geophys. Res. Lett.*, *36*, L03304, doi:10.1029/2008GL036407.
- Miller, M. S., B. L. N. Kennett, and V. G. Toy (2006), Spatial and temporal evolution of the subducting Pacific plate structure along the western Pacific margin, *J. Geophys. Res.*, *111*, B02401, doi:10.1029/2005JB003705.
- Montelli, R., G. Nolet, F. A. Dahlen, G. Masters, E. R. Engdahl, and S.-H. Hung (2004), Finite-frequency tomography reveals a variety of plumes in the mantle, *Science*, *303*, 338–343.
- Paige, C. C., and M. A. Saunders (1982), LSQR: An algorithm for sparse linear equations and sparse least squares, *ACM Trans. Math. Software*, *8*, 43–71.
- Ren, Y., E. Stutzmann, R. D. van der Hilst, and J. Besse (2007), Understanding seismic heterogeneities in the lower mantle beneath the Americas from seismic tomography and plate tectonic history, *J. Geophys. Res.*, *112*, B01302, doi:10.1029/2005JB004154.
- Replumaz, A., H. Kárason, R. D. van der Hilst, P. Tapponnier, and J. Besse (2004), 4-D evolution of SW Asia mantle structure from geological reconstructions and seismic tomography, *Earth Planet. Sci. Lett.*, *221*, 101–115.
- Resovsky, J., and J. Trampert (2003), Using probabilistic seismic tomography to test mantle velocity-density relationships, *Earth Planet. Res. Lett.*, *215*, 121–134.
- Ricard, Y., M. Richards, C. Lithgow-Bertelloni, and Y. Le Stunff (1993), A geodynamic model of mantle density heterogeneity, *J. Geophys. Res.*, *98*, 21,895–21,909.
- Richards, M. A., and D. C. Engebretson (1992), Large-scale mantle convection and the history of subduction, *Nature*, *355*, 437–440.
- Ritsema, J., H. J. van Heijst, and J. H. Woodhouse (2004), Global transition zone tomography, *J. Geophys. Res.*, *109*, B02302, doi:10.1029/2003JB002610.
- Röhm, A., J. Trampert, H. Paulssen, and R. Snieder (1999), Bias in reported seismic arrival times deduced from the ISC catalogue, *Geophys. J. Int.*, *137*, 163–174.
- Saltzer, R., R. D. van der Hilst, and H. Kárason (2001), Comparing P and S wave heterogeneity in the mantle, *Geophys. Res. Lett.*, *28*, 1335–1338.
- Saltzer, R., E. Stutzmann, and R. D. van der Hilst (2004), Poisson's ratio in the lower mantle beneath Alaska: Evidence for compositional heterogeneity, *J. Geophys. Res.*, *109*, B06301, doi:10.1029/2003JB002712.
- Soldati, G., and L. Boschi (2005), The resolution of whole Earth seismic tomographic models, *Geophys. J. Int.*, *161*, 143–153.
- Soldati, G., L. Boschi, and A. Piersanti (2006), Global seismic tomography and modern parallel computers, *Ann. Geophys.*, *49*, 977–986.
- Spakman, W., and G. Nolet (1988), Imaging algorithms, accuracy and resolution in delay time tomography, in *Mathematical Geophysics: A Survey of Recent Developments in Seismology and Geodynamics*, edited by N. J. Vlaar, pp. 155–188, D. Reidel, Hingham, Mass.
- Spakman, W., S. Stein, R. van der Hilst, and R. Wortel (1989), Resolution experiments for NW Pacific subduction zone tomography, *Geophys. Res. Lett.*, *16*, 1097–1100.
- Su, W.-J., and A. M. Dziewonski (1997), Simultaneous inversion for 3-D variations in shear and bulk velocity in the mantle, *Phys. Earth Planet. Inter.*, *100*(1–4), 135–156.
- Tarantola, A. (2005), *Inverse Problem Theory and Methods for Model Parameter Estimation*, Soc. for Ind. and Appl. Math., Philadelphia, Pa.
- Trampert, J., and J. J. Lévêque (1990), Simultaneous iterative reconstruction technique: Physical interpretation based on the generalized least squares solution, *J. Geophys. Res.*, *95*, 12,553–12,559.
- Trampert, J., and R. D. van der Hilst (2005), Towards a quantitative interpretation of global seismic tomography, in *Earth's Deep Mantle: Structure, Composition, and Evolution*, *Geophys. Monogr. Ser.*, vol. 160, edited by R. D. van der Hilst et al., pp. 47–62, AGU, Washington, D. C., doi:10.1029/160GM05.
- van der Hilst, R. D. (1995), Complex morphology of subducted lithosphere in the mantle beneath the Tonga trench, *Nature*, *374*, 154–157.
- van der Hilst, R. D., and T. Seno (1993), Effects of relative plate motion on the deep structure and penetration depth of slabs below the Izu-Bonin and Mariana island arcs, *Earth Planet. Res. Lett.*, *120*(3–4), 395–407.
- van der Hilst, R. D., E. R. Engdahl, W. Spakman, and G. Nolet (1991), Tomographic imaging of subducted lithosphere below northwest Pacific island arcs, *Nature*, *353*, 37–42.
- van der Hilst, R. D., E. R. Engdahl, and W. Spakman (1993), Tomographic inversion of P and pP data for aspherical mantle structure below the northwest Pacific region, *Geophys. J. Int.*, *115*, 264–302.
- van der Hilst, R. D., S. Widiyantoro, and E. R. Engdahl (1997), Evidence for deep mantle circulation from global tomography, *Nature*, *386*, 578–584.
- van der Voo, R., W. Spakman, and H. Bijwaard (1999), Tethyan subducted slabs under India, *Earth Planet. Sci. Lett.*, *171*, 7–20.
- Vasco, D. W., and L. R. Johnson (1998), Whole Earth structure estimated from seismic arrival times, *J. Geophys. Res.*, *103*(B2), 2633–2671.

- Vasco, D. W., L. R. Johnson, and O. Marques (2003), Resolution, uncertainty, and whole Earth tomography, *J. Geophys. Res.*, *108*(B1), 2022, doi:10.1029/2001JB000412.
- Widiyantoro, S., A. Gorbato, B. L. N. Kennett, and Y. Fukao (2001), Improving global shear wave traveltimes tomography using three-dimensional ray tracing and iterative inversion, *Geophys. J. Int.*, *141*(3), 747–758.
- Wolfe, C. J., S. C. Solomon, P. G. Silver, J. C. VanDecar, and R. M. Russo (2002), Inversion of body-wave delay times for mantle structure beneath the Hawaiian islands: Results from the PELENET experiment, *Earth Planet. Res. Lett.*, *198*, 129–145.
- Wolfe, C. J., S. C. Solomon, G. Laske, J. A. Collins, R. S. Detrick, J. A. Orcutt, D. Bercovici, and E. H. Hauri (2009), Mantle shear-wave velocity structure beneath the Hawaiian hot spot, *Science*, *326*, 1388–1390.
- Zhao, D. (2004), Global tomographic images of mantle plumes and subducting slabs: Insight into deep Earth dynamics, *Phys. Earth Planet. Inter.*, *146*, 3–34.
- 
- R. W. L. de Wit and J. Trampert, Department of Earth Sciences, Utrecht University, Budapestlaan 4, NL-3508 TA Utrecht, Netherlands. (rdewit@geo.uu.nl; jeannot@geo.uu.nl)
- R. D. van der Hilst, Department of Earth, Atmospheric, and Planetary Sciences, Massachusetts Institute of Technology, Cambridge, MA 02139, USA. (hilst@quake.mit.edu)